Original Article

5T magnetic resonance imaging: radio frequency hardware and initial brain imaging

Zidong Wei[1,2,3,4#], Qiaoyan Chen[1,2#], Shihong Han[4], Shuheng Zhang[4], Na Zhang[1,2], Lei Zhang[1,2], Haining Wang[4], Qiang He[4], Peng Cao[5], Xiaoliang Zhang[6], Dong Liang[1,2], Xin Liu[1,2], Ye Li[1,2], Hairong Zheng[1,2]

[1]Paul C. Lauterbur Research Center for Biomedical Imaging, Shenzhen Institute of Advanced Technology, Chinese Academy of Sciences, Shenzhen, China; [2]The Key Laboratory for Magnetic Resonance and Multimodality Imaging of Guangdong Province, Shenzhen, China; [3]University of Chinese Academy of Sciences, Beijing, China; [4]Shanghai United Imaging Healthcare, Shanghai, China; [5]Department of Diagnostic Radiology, The University of Hong Kong, Hong Kong, China; [6]Department of Biomedical Engineering, State University of New York at Buffalo, Buffalo, NY, USA

Contributions: (I) Conception and design: Z Wei, Q Chen, Y Li, H Zheng; (II) Administrative support: H Wang, Q He, D Liang, X Liu, Y Li, H Zheng; (III) Provision of study materials or patients: H Wang, Q He, D Liang, X Liu; (IV) Collection and assembly of data: Z Wei, Q Chen, S Han, S Zhang, N Zhang, L Zhang, P Cao; (V) Data analysis and interpretation: Z Wei, Q Chen, S Han, S Zhang, N Zhang, L Zhang, X Zhang, Y Li, H Zheng; (VI) Manuscript writing: All authors; (VII) Final approval of manuscript: All authors.

[#]These authors contributed equally to this work.

Correspondence to: Ye Li, PhD; Hairong Zheng, PhD. Paul C. Lauterbur Research Center for Biomedical Imaging, Shenzhen Institute of Advanced Technology, Chinese Academy of Sciences, and the Key Laboratory for Magnetic Resonance and Multimodality Imaging of Guangdong Province, Shenzhen 518055, China. Email: liye1@siat.ac.cn; hr.zheng@siat.ac.cn.

Background: We aimed to demonstrate the feasibility of generating high-resolution human brain magnetic resonance imaging (MRI) at 5 Tesla (T) using a quadrature birdcage transmit/48-channel receiver coil assembly.

Methods: A quadrature birdcage transmit/48-channel receiver coil assembly was designed for human brain imaging at 5T. The radio frequency (RF) coil assembly was validated by electromagnetic (EM) simulations and phantom imaging experimental studies. The simulated B1+ field inside a human head phantom and inside a human head model generated by the birdcage coils driven in circularly polarized (CP) mode at 3T, 5T and 7T was compared. Signal-to-noise ratio (SNR) maps, the inverse g-factor maps for evaluation of parallel imaging performance, anatomic images, angiography images, vessel wall images and susceptibility weighted images (SWI) were acquired using the RF coil assembly at 5T and compared to those acquired using a 32-channel head coil on a 3T MRI scanner.

Results: For the EM simulations, 5T MRI provided less RF inhomogeneity compared to that of 7T. In the phantom imaging study, the distributions of the measured B1+ field were consistent with the distributions of the simulated B1+ field. In the human brain imaging study, the average SNR value of the brain in the transversal plane at 5T was 1.6 times of that at 3T. The 48-channel head coil at 5T had higher parallel acceleration capability than the 32-channel head coil at 3T. The anatomic images at 5T also showed higher SNR than those at 3T. Improved delineation of the hippocampus, lenticulostriate arteries, and basilar arteries was observed at 5T compared to 3T. SWI with a higher resolution of 0.3 mm ×0.3 mm ×1.2 mm could be acquired at 5T, which enabled better visualization of small blood vessels compared to that at 3T.

Conclusions: 5T MRI can provide significant SNR improvement compared to that of 3T with less RF inhomogeneity than that of 7T. The ability to obtain high quality in vivo human brain images at 5T using the quadrature birdcage transmit/48-channel receiver coil assembly has significant in clinical and scientific research applications.

Keywords: Brain imaging; magnetic resonance imaging; ultrahigh field; 5T; high quality imaging

Submitted Sep 09, 2022. Accepted for publication Mar 13, 2023. Published online Mar 29, 2023.
doi: 10.21037/qims-22-945
View this article at: https://dx.doi.org/10.21037/qims-22-945

Introduction

Magnetic resonance imaging (MRI) is the reference standard for the assessing neurological disorders that are the leading cause of disability and the second leading cause of death globally (1). MRI is also one of the most important diagnostic methods for systemic diseases due to its unparalleled soft tissue contrast. Better image quality and higher spatial resolution can be achieved in these assessments by using advanced technologies in MRI pulse sequences and hardware, including higher field strengths (2). The ultrahigh field [>3 Tesla (T)] MRI systems have important technical advantages including spatial resolutions as high as 100–200 microns for some applications. They can observe microscopic structures, functional nuclei, and molecular metabolism. Using ultrahigh field MRI systems can enable the study of the relationship between structure and function of biological tissues from the perspectives of molecular imaging, physiology and metabolism (3). Such systems can also enable to explore the mechanism and pathological process of major diseases such as tumor (4).

Increasing the magnetic field strength of MRI systems not only improves signal-to-noise ratio (SNR) to obtain high resolution images (5-9), but also increases susceptibility-based contrasts in anatomical and functional imaging (10,11). Because of its high sensitivity to tissue susceptibility, ultrahigh field MRI also demonstrates potential for high resolution susceptibility weighted images (SWI) (11), which is applied for assessments of cerebral veins, stroke, multiple sclerosis, tumors or hemorrhagic lesions. These observations have resulted in a push for higher field MRI systems (12-14).

However, due to regulation issues, the clinical use of ultra-high field MRI systems has been limited until recently. Although relatively recent the Food and Drug Administration (FDA) approval/ European conformity (CE) mark might change this, it should be noted that restrictions still apply to the approved setups. Furthermore, as the radio frequency (RF) wavelength becomes shorter than the dimensions of the object being imaged, the B_1^+ field shows inhomogeneity due to constructive and destructive magnetic field interferences in ultrahigh field MRI scanners (15,16). This problem has been solved by using parallel transmit RF coils with B_1^+ phase and/or amplitude shimming (17-19), and pulse sequences such as transmit sensitivity encoding (20-23), spoke pulses (24-27), and k-T pulses (28). These advances generate uniform flip angles over an imaged region. However, the supervision of multichannel transmit coils is more complicated with independent time-varying amplitudes and phases in the ultrahigh MRI systems, primarily due to a higher dependence on the patient's anatomy (29). In combination with B_1^+ field inhomogeneity, RF power transfer causes an increase in the body's core temperature, which is a major concern in ultrahigh MRI. This transfer is defined by the specific absorption rate (SAR, measured in W/kg) and SAR increases quadratically with the strength of the main magnetic field (30,31). Measures that can be taken to reduce SAR have been described (17,32,33). Nevertheless, for only head MRI, International Electrotechnical Commission (IEC) guidelines recommend a global SAR limit of 3.2 W/kg for body transmit coils and a local SAR limit of 10 W/kg for local transmit coils in the normal operating mode (34).

Despite 20 years of development, these issues limited the clinical use of ultrahigh field MRI. So far, the most commonly used clinical MRI system is the 3T MRI scanners. An intermediate magnetic field strength of 5T may provide significant SNR improvement above 3 T, but avoids some of the more sticky issues of today's 7T (and higher) systems (35), such as RF-related issues. Previously, a 4.7T whole-body MRI system was built and used for human brain imaging (36,37), equipped with shielded head gradient coil with gradient fields of up to 36 mT/m and a maximum slew rate of 195 mT/m/ms, and a transmit/receive four-port drive birdcage RF coil (37). However, such a configuration is not optimal based on current MRI technology. Better image quality and higher image resolution can be achieved using a high density receiver coil array in combination with parallel imaging techniques.

Typically, SNR and parallel imaging performance can be improved by increasing the channel number of RF receiver

coils. At 3T, the channel count of the commercially available head coils is 32 (38), 48 (39) or 64 (40). However, the size of the coils progressively decreases when the channel number of receiver coils increases, causing the thermal noise from the coil to be dominant. Thus, the SNR improvement is limited by using this approach (41,42). This problem is less pronounced at ultrahigh field MRI because the thermal noise from the sample also increases with the magnetic field strength and can remain the predominant contribution of the niose (43). Therefore, a head coil with a high channel count at 5T would demonstrate a better parallel imaging performance compared with the commercially available head coils at 3T.

In this work, we designed and constructed a 48-channel RF receiver array combined with a local birdcage transmit coil for human brain imaging on a prototype 5T whole-body MRI scanner. First, the RF coil assembly was validated by electromagnetic (EM) simulations and phantom imaging experimental studies, of which the simulated and measured B_1^+ fields were shown to demonstrate consistency. Additionally, the simulated B_1^+ field inside a human head phantom and inside a human head model generated by the birdcage coils driven in circularly polarized (CP) mode at 3T, 5T and 7T was compared. Then, SAR distributions at 5T were investigated in 12 different head models during a safety assessment. Finally, SNR maps, the inverse g-factor maps to evaluate the parallel imaging performance, anatomic images, angiography images, vessel wall images, and SWI were acquired using the RF coil assembly at 5T and compared to those acquired using a 32-channel head coil on a 3T MRI scanner.

Methods

The 5.0 T MRI scanner

MRI experiments were performed on a novel whole body 5.0 T MRI scanner (MR 5.0 T, United Imaging Healthcare, Shanghai, China) with a clear bore that was 60 cm in diameter. The field homogeneity of the main magnet was about 0.02 ppm over an empty sphere with a 20 cm diameter. The gradient system was driven by a 3.5 MW power amplifier, equipped with a maximum gradient strength of 120 mT/m and a slew rate of 200 T/m/s. The scanner was equipped with 96 receivers and 8-channel parallel transmitter that was independently driven by an RF power amplifier with a peak power of 8 kW.

RF coil design and construction

In this study, a local birdcage transmit coil and a 48-channel receiver coil were constructed (*Figure 1*). The local high-pass birdcage transmit coil was driven in CP mode, of which the circuit schematic is shown in *Figure 1D*. The high-pass birdcage coil had one cut in the rungs. Positive-intrinsicnegative (PIN) diodes (Macom, MA4P7435NM-1091T) were added to the cuts and the ports of the transmit coil to enable active detuning during signal reception. The shielded transmit coil had a 30 cm diameter, and was comprised of 16 rungs, each with a length of 28 cm and a shield with a diameter of 34 cm. The diameter of the shielding was chosen based on the requirement for the coil center and shield center to be in line with the magnet center. To prevent the eddy current problem, the shielding was slit and divided into 32 strips, connected through capacitors (1 nF). The transmit coil conductor was copper that was 35 μm thick and 10 mm wide. The conductor had a 0.1 mm thick on an FR4 substrate.

The receiver coil was arranged on a close-fitting helmet with inner dimensions of 230 mm in the antero-posterior (AP) direction, 210 mm in the left-right (LR) direction, and 266 mm in the inferior-superior (IS) direction. 16 elements in 3 rows were anterior and 32 elements in 5 rows were posterior, as shown in *Figure 1C*. In the receiver coil, the opening for the eyes was located in the position of elements 2 and 3, which were larger than the other elements. A mirror could be mounted on the opening, as shown in *Figure 1A*, which could be used to study some visual brain functions. The helmet shape was designed to accommodate the 90th percentile contour of the standard head norm, and was fabricated using acrylonitrile butadiene styrene plastic. The anterior head segment was integrated with the transmit coil and overlapped the posterior head segment to allow the receiver loops on the two halves to be geometrically decoupled. The channels were loops of copper with 35 μm thick and 5 mm wide. The sizes of each loop element was 65–75 mm in length, and they were approximately rectangular in shape. A combination of inductive and geometrical decoupling was used to cancel the inductive coupling between neighboring loops. The next-nearest neighboring loops were decoupled using preamplifier decoupling.

The circuit schematic of the receiver elements is shown in *Figure 1E*. The receive elements included a tuning circuit, a matching circuit, a passive detune circuit and an active detune circuit. Each element was tuned to a

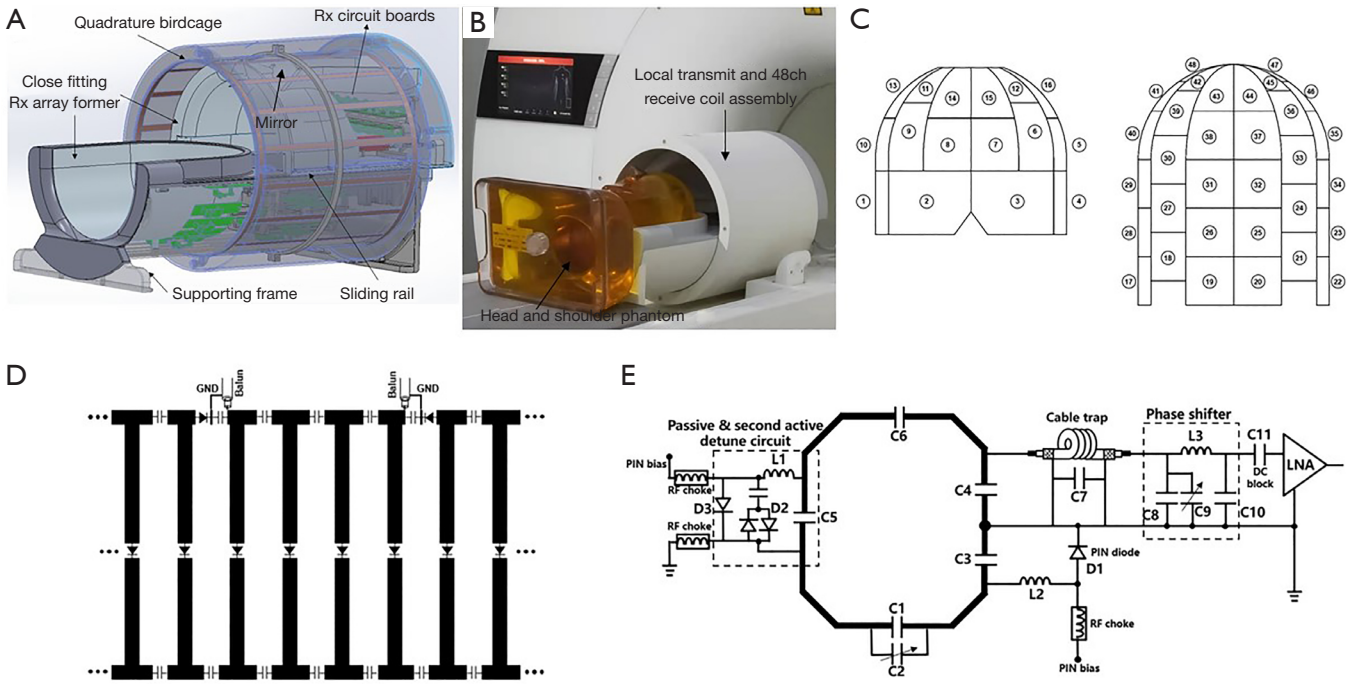

Figure 1 The quadrature birdcage transmit/48-channel receiver coil assembly at 5T. (A) the layout of the coil assembly; (B) the photograph of the coil assembly; (C) the layout of the 48-channel receive coil; (D) the circuit schematic of the transmit birdcage coil; (E) the circuit schematic of a receiver coil element.

Larmor frequency of 210.8 MHz, and the impedance was matched to 50 Ω. To reduce the influence of the current flow in the receiver coil during transmit operation, a two-stage detuning circuit was designed for primary protection levels. PIN diodes were switched on via the current source when the transmit was switched on. The first active detune circuit comprised a PIN diode D1 (Macom, MA4P7435NM-1091T), an inductance L2, and a capacitor C3. The second active detune circuit comprised a PIN diode D3 (Macom, MA4P7435NM-1091T), an inductor L1, and a capacitor C5. For secondary protection levels, the passive detune circuit was composed of a capacitor C5, an inductance L1, and an antiparallel diode pair D2 (Microsemi, UMX9989AP). The cable length and phase shifter were carefully adjusted for each loop to achieve preamplifier decoupling. To minimize Hall effects within the field-effect transistors in the preamplifier and to protect the preamplifier from the risk of being damaged during RF transmission, most of the home-made preamplifiers (gain ≥25 dB; Noise figure ≤0.5 dB; input impedance <2 Ω) were oriented in the z direction and positioned outside the transmit coil. The transmit and receiver coil assembly was connected via the plugs at the head end of the patient table.

Bench testing was implemented using a custom-made test power supply and a vector network analyzer (Agilent, E5061B), including the tuning, matching, active detuning, and decoupling of the coil elements. The custom-made test power supply provided 6.5 V for the preamplifiers. It tuned the local transmit coil and detuned the receiver coil using a switch to bias PIN diodes with a 150 mA current during the transmit mode. It also detuned the local transmit coil and tuned the receiver coil using a switch to reverse biasing of the diodes with a - 30 V voltage during image acquisition. The S11 parameter values were measured to evaluate the tuning and matching of the individual elements using the vector network analyzer. For the evaluation of the decoupling, the S21 parameter values were measured using cables directly connected to the preamplifier sockets of the two adjacent or nonadjacent coil elements on the vector network analyzer. During the decoupling test, the preamps were attached to supply preamplifier decoupling and all the other coil elements were actively detuned with the PIN

diode under forward bias.

RF coil validation and SAR safety

Before *in vivo* imaging, the RF coil assembly needed to be validated (33). First, EM simulations and phantom imaging experimental studies were used to demonstrate the consistency of the simulated and measured B_1^+ fields. The EM simulation was performed using the finite-integration time-domain method (Microwave Studio, CST, Darmstadt, Germany) with a broadband Gaussian excitation at a center frequency of 210.8 MHz, and the bandwidth was 200 MHz. The three-dimensional (3D) EM model of the transmit coil was simulated with precise dimensions. In the simulation, the conductor material of the transmit coil was defined as pure copper, and the series resistances of the PIN diodes and equivalent series resistance for the lossy capacitance were set to 0.2 Ω and 0.1 Ω, respectively. The coil shield was included in the simualtion, but the receiver coil loops, cable trap, and DC wiring were not. The transmit coil was tuned to 210.8 MHz and matched to 50 Ω with a reflection parameter less than –15 dB. The B_1^+ maps were normalized to the coil accepted input power.

We compared the simulated B_1^+ field inside a human head phantom and inside a human head model (Gustav, the commonly used male model) generated by the birdcage coils driven in CP mode at 3T, 5T and 7T. The human head phantom was built based on the three-dimensional shape of a human head, as shown in *Figure 1B*. It was filled with 523.8 g/L polyvinylpyrrolidone and 11.5 g/L sodium chloride (44) to mimic the average dielectric properties of human brain tissue, of which the conductivity is 0.53 s/m and the relative permittivity is 55.4 at 210.8 MHz. The 3T MRI scanner (uMR790, United Imaging Healthcare, Shanghai, China) was outfitted with a body transmit coil and a 32-channel head receiver coil (45). For the 32-channel head coil at 3T, 14 elements in four rows were anterior and 18 elements in four rows were posterior. The inner dimensions of the 32-channel head coil at 3T were: 230 mm in the AP direction, 210 mm in the LR direction, and 260 mm in the IS direction. The head receiver coils at 5T and 3T had similar inner dimensions. The birdcage coil at 3T comprised 32 rungs and had a 62 cm diameter and a 45 cm length, of which the coil conductor was 35 μm thick and 32 mm wide. The coil shield at 3T had a 66.8 cm diameter and a 140 cm length. The size of the birdcage transmit coil at 7T was set as the same as that at 5T for a fair comparison. In the human head model and human head phantom simulations, the dielectric parameters were based on the Gabriel dispersion relationship (46).

In the B_1^+ field measurements, the receiver coil was assembled within the transmit coil. The B_1^+ maps were acquired using a dual refocusing echo acquisition mode (DREAM) sequence with the following parameters: time of relaxation (TR) =3,000 ms; time of echo (TE) =1.49 ms; flip angle =54.7°; slice thickness =10 mm; field of view (FOV) =300×300 mm^2; and matrix size =84×84. The simulated and measured B_1^+ field maps were constructed by normalizing the accepted input power. Mean and relative standard deviation (RSD) values were calculated in the region of interest. Notably, the $B1^+$ field maps were constructed after a -4 dB transmission loss from the RF amplifiers to the coil plugs, and a -0.3 dB loss from coil plugs to the matched coils. The simulated and measured B_1^+ field maps included these losses.

EM simulations in 12 human head models were performed to determine safety total power limits and evaluate local SAR_{10g} values in operation. In our CST version (CST studio suite 2021, Dassault Systèmes, French), only 6 adult human models (Emma, Gustav, Hugo, Donna, Laura, and Katja) were available. In our sim4life version (V6.2, Zurich Med Tech, Switzerland), only 6 adult human models (Ella, Ella30, Duke, Fats, Fats29, and Glenn) were available. In order to increase the models for SAR simulations, we used both software for analysis, which can provide a greater security guarantee. Whole-head and peak SARs arising from the transmit coil in CP mode with a total input power of 1 W were averaged over 10 g of tissue (SAR_{10g}) in each head model.

In the 5T MRI system, a directional coupler was used to measure and monitor the transmitted RF power. The directional coupler was connected in series at the transmit power amplifier to detect the forward power and reverse power. The applied power was collected in real time by combining it with the analog-to-digital converter. The relationship between the total power exposed in head tissues (W) and the total incident power using power monitors (W_t) was given by:

$$W = W_t\left(1-\frac{Q_{load}}{Q_{unload}}\right) = \eta W_t \quad [1]$$

$$\eta = \left(1-\frac{Q_{load}}{Q_{unload}}\right) \quad [2]$$

Where Q_{load} and Q_{unload} are the head coil quality factor

Table 1 Typical sequence parameters

	Sequence	TR (ms)	TE (ms)	FA (°)	Average	PPA (CS)	BW (Hz/pixel)	Acquired resolution (mm^3)	Reconstructed resolution (mm^3)	TA (min)
5T	GRE	3,000	6.5	30	1	0	590	1.95×1.95×5.0	1.95×1.95×5.0	6
	T2_FSE	4,300	115.4	100	4	2	230	0.3×0.3×2.5	0.15×0.15×2.5	6.8
	TOF	20	4	15	1	3.5	210	0.5×0.5×0.5	0.25×0.25×0.25	11.13
	T1_mx3d	830	15	74	1	6	440	0.5×0.5×0.5	0.3×0.3×0.3	7.17
	SWI	27	16	10	1	3	120	0.5×0.5×1.0	0.5×0.5×0.5	7
	SWI	30	16	10	1	3	100	0.3×0.3×1.2	0.15×0.15×0.6	13.17
3T	GRE	3,000	6.5	30	1	0	590	1.95×1.95×5.0	1.95×1.95×5.0	6
	T2_FSE	4,700	128.7	100	4	2	230	0.3×0.3×2.5	0.15×0.15×2.5	6.8
	TOF	16	3.5	15	1	3	260	0.5×0.5×0.5	0.25×0.25×0.25	10.67
	T1_mx3d	800	16.2	75	1	5.4	440	0.5×0.5×0.5	0.3×0.3×0.3	6.87
	SWI	28	18	15	1	3	130	0.5×0.5×1.0	0.5×0.5×0.5	7

TR, time of relaxation; TE, time of echo; FA, flip angle; PPA, partially parallel acceleration; CS, compressed sensing; BW, bandwidth; TA, time of acquisition; GRE, gradient echo; T2_FSE, T2-weighted fast spin echo; TOF, time of flight; T1_mx3d, T1-weighted three-dimensional MATRIX (Modulated flip Angle Technique in Refocused Imaging with eXtended echo train) sequence; SWI, susceptibility weighted images.

(Q) measured in the presence and absence of the subject, and η is defined as the coefficient of the energy absorption in the tissues. Here, the Q value was measured using the dual-loop probe method (47). During the measurement, the two pickup loops were placed inside the transmit coil, on the middle of each side of the shell. The Q factor is defined as (47):

$$Q = \frac{f_0}{B_W} \quad [3]$$

Where f_0 is the resonant frequency of the coil, and B_W is the -3 dB bandwidth of the S21 parameter.

In the experimental studies, the total SAR deposited in the tissue was estimated by measuring the total incident power using power monitors on the 5T MRI scanner. During the scan, there would be a cross-section of SAR monitoring to view the total SAR. The calculated peak SAR could be obtained by using the following formula:

$$SAR_{peak} = SAR_{total} \cdot \eta \cdot w_{\max} \quad [4]$$

Where $w_{\max}$ was the max ratio of peak SAR_{10g} to total SAR_{10g} in the 12 simulations.

In vivo human brain imaging

This study was approved by the institutional review board of Shenzhen Institutes of Advanced Technology, Chinese Academy of Sciences. And the study conformed to the provisions of the Declaration of Helsinki (as revised in 2013). Informed consent was obtained from all the volunteers before the human studies were implemented. In this study, since each experiment took a long time, we divided the volunteers into groups according to the experiment's content and time. A total of four healthy volunteers were scanned. SNR maps were obtained from a 30 years old healthy volunteer (male; 160 cm; 65 kg). Fast spin echo (FSE) brain images were obtained from a 37 years old healthy volunteer (male; 170 cm; 70 kg). Magnetic resonance angiography (MRA) images were obtained from a 28 years old healthy volunteer (male; 170 cm; 52 kg). Vascular wall images and SWI were obtained from a 39 years old healthy volunteer (male; 170 cm; 80 kg).

For SNR comparisons, a two-dimensional (2D) density-weighted gradient echo (GRE) sequence was applied for signal acquisition using the following parameters shown in *Table 1*. Noise images were acquired by setting the flip angle

to 0°. SNR maps were calculated using the sum-of-squares method on the data from each scanner, then compared (48).

For a RF-spoiled GRE acquisition, the SNR was given by (9):

$$SNR = SNR_0 \cdot S_C \cdot \frac{1-e^{-TR/T1}}{1-\cos\alpha \cdot e^{-TR/T1}} \cdot \sin\alpha \cdot e^{-TE/T2^*} \quad [5]$$

where T1 is the longitudinal transverse relaxation time and T2* is the apparent transverse relaxation time. TR and TE are the repetition time and the echo time of the RF-spoiled GRE sequence, respectively. α represents the flip angle. S_C is the sensitivity of the receiver coil, including the noise figure of the receiver chain. The theoretical estimation of SNR_0 was obtained with this equation.

The flip angle maps used a B_1^+ mapping DREAM sequence with the following parameters: TR =3,000 ms; TE =1.49 ms; flip angle =54.7°; slice thickness =10 mm; FOV =250×250 mm^2; and matrix size =80×80. For T2* mapping, a multiecho GRE sequence was used with 12 echo times between 5 ms and 53 ms. The parameters were shown as follows: TR =3,000 ms; flip angle =30°; slice thickness =5 mm; FOV =250×250 mm^2; and matrix size =128×128. T2* maps were obtained using polynomial curve fitting with the multiecho data for every voxel in the Matlab software (MathWorks, United States). For T1 mapping, a 2D spin-echo inversion recovery (SE-IR) sequence was used. The protocol was: FOV =250×250 mm^2; matrix size =128×128; slice thickness =5 mm; TR =10 s; TE =10 ms; bandwidth =500 Hz/pixel; and 9 inversion times TIs: 100, 200, 300, 500, 1,000, 1,500, 2,000, 2,500 and 3,000 ms. To obtain T1 maps, the following equation was applied to fit the relaxation curve (9):

$$M(TI) = M_0 \cdot \left(1-2\beta e^{-TI/T1}\right) \quad [6]$$

After the calculations of the T2* and T1 maps, the T2* and T1 values of the white and gray matter were calculated by taking the mean of two regions of interest (ROI) with 5×5 pixels, respectively. To evaluate parallel imaging capability, the inverse g-factor maps were analyzed using sensitivity encoding (SENSE) reconstructions (49). The inverse g-factor maps were evaluated with the acceleration factors *R* ranging from 2 to 6 in the AP direction, *R* =2×2 and *R* =3×3 in two directions (AP and LR).

Anatomic images were obtained using a T2-weighted fast spin echo (T2_FSE) sequence. MRA images were obtained using a time of flight (TOF) sequence. Vascular wall images were acquired using a T1-weighted 3D MATRIX (Modulated flip Angle Technique in Refocused Imaging with eXtended echo train) sequence (T1_mx3d). Lenticulostriate arteries (LSAs) were particularly visualized, which are one of the most important vascular structures in the human brain and the sites of many neurological diseases (50). SWI images were acquired with resolutions of 0.5 mm × 0.5 mm × 1.0 mm and 0.3 mm × 0.3 mm × 1.2 mm using the 5T MRI scanner, and with a resolution of 0.5 mm × 0.5 mm × 1.0 mm using the 3T MRI scanner. The typical sequence parameters are shown in *Table 1*.

Results

The simulated B_1^+ field maps in the transversal, sagittal, and coronal planes at 3T, 5T and 7T were calculated, as shown in *Figure 2*. The mean and RSD values in the region of interest (dotted circle) are depicted in the maps. The B_1^+ maps at 3T were the most homogeneous, and the B_1^+ maps at 5T were more homogeneous than those at 7T. In the human head model (Gustav), the homogeneity of the simulated B_1^+ field at 5T, represented by the RSD value, could be improved by more than 26% compared to that at 7T.

The measured B_1^+ field maps inside the human head phantom at 5T were constructed in the transversal, sagittal, and coronal planes, as shown in *Figure 3*. The mean and RSD values in the region of interest (dotted circle) are depicted in the maps. The distributions of the measured B_1^+ field were consistent with the distributions of the simulated B_1^+ field depicted in *Figure 2*.

The total SAR and peak SAR_{10g} values in simulations using the head models at 5T are summarized in *Table 2*. The intersubject local SAR variability range was 0.3765 W/kg±19% (0.305–0.448 W/kg) for the peak SAR_{10g} with 1 W input power. If the Glenn head model was used to define safe power limits, the peak SAR_{10g} value achieved by the Laura head model could be 47% higher than predicted. Thus, for the peak SAR_{10g} evaluation using only 1 head model, the required safety margin to account for the intersubject variability is 1.47 at minimum. In the 12 simulations, the max ratio of peak SAR_{10g} to total SAR_{10g} was 3.64, which could be used for the evaluation of the worst case SAR.

The measured S11 and S22 parameters of the transmit birdcage coil loading with the human head phantom were about -13 dB and -17 dB, respectively, and had 10 dB return loss bandwidths of 3.51 MHz and 3.92 MHz, respectively.

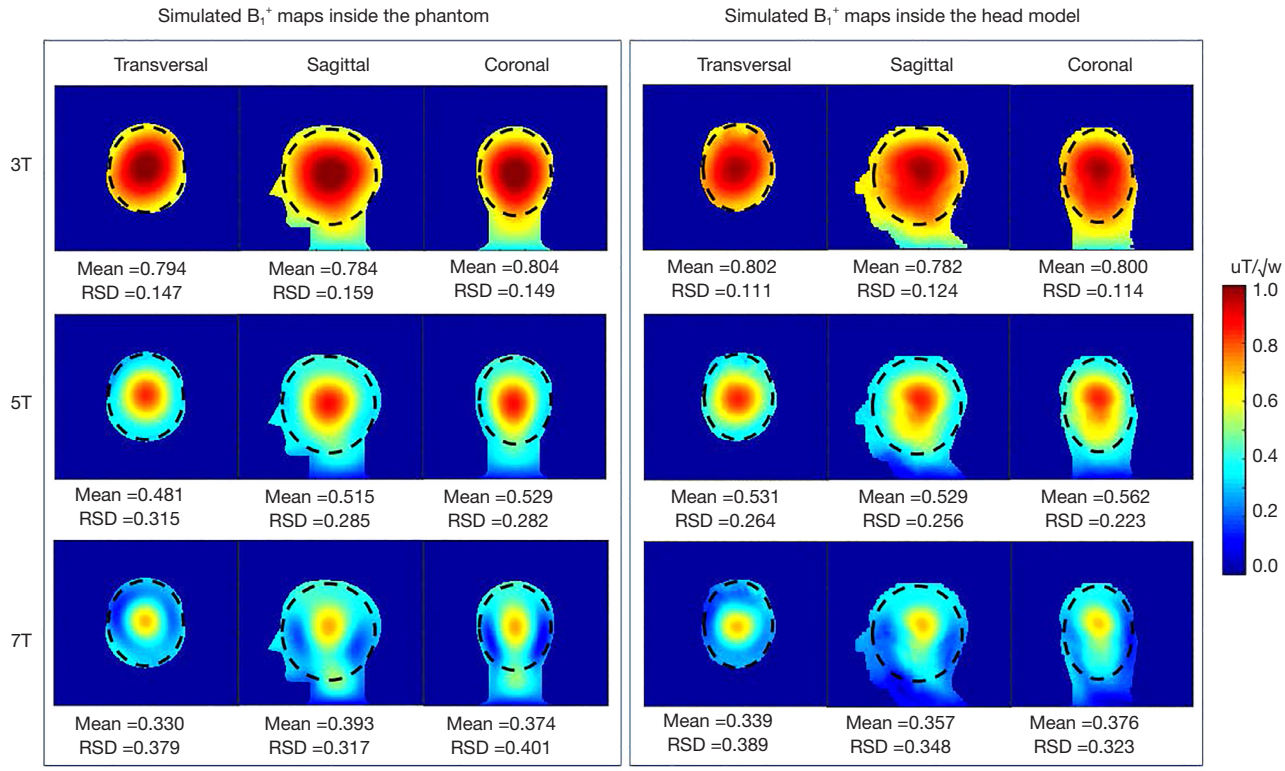

Figure 2 Simulated B1+ field maps at 3T, 5T and 7T inside the human head phantom and the human head model (Gustav). In the figure, mean and RSD represent the mean and relative standard deviation values in the region of interest (dotted circle), respectively.

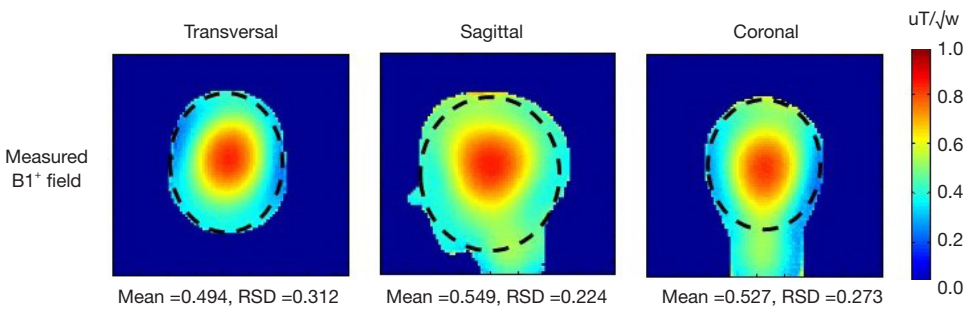

Figure 3 Measured B1+ field maps inside the human head phantom at 5T in the phantom. In the figure, mean and RSD represent the mean and relative standard deviation values in the region of interest (dotted circle), respectively.

The quality factor of the transmit coil measured in the absence of the subject was Q_{unload}=60.23, and it was Q_{load}=21.29 when the transmit coil loaded with a human subject, using the dual-probe method. The coefficients of the energy absorption in the tissues was 64.65%, calculated by using equation (2). In the experimental studies, the total SAR deposited in the tissue was estimated by measuring the total incident power using power monitors on the 5T MRI scanner. Based on the simulations, the max ratio of peak SAR_{10g} to total SAR_{10g} was 3.64. The calculated peak SAR was obtained by using Eq. [3], which was used to determine whether it meets the IEC guidelines (51).

The S11 parameters of six representative coil elements (2, 8, 9, 14, 32 and 44) were −5, −20, −22, −16, −14 and −20 dB at 210.8 MHz, respectively. The S21 parameter of six representative neighboring coil elements (31, 32, 37, 38,

Table 2 The total and peak SAR_{10g} values in simulations using the head models at 5T

Model	Age (year)	Gender	Body mass index (kg/m^2)	Total SAR (W/kg)	Peak SAR_{10g} (W/kg)	Peak SAR_{10g}/total SAR
Emma	26	Female	28.0	0.141	0.444	3.15
Gustav	38	Male	22.3	0.146	0.431	2.95
Hugo	38	Male	31.8	0.128	0.403	3.15
Donna	40	Female	25.5	0.114	0.389	3.41
Laura	43	Female	19.2	0.143	0.448	3.13
Katja	43	Female	23.3	0.162	0.388	2.40
Ella	26	Female	21.6	0.112	0.408	3.64
Ella30	26	Female	30.0	0.120	0.378	3.15
Duke	34	Male	22.4	0.130	0.346	2.66
Fats29	37	Male	29.0	0.105	0.375	3.57
Fats	37	Male	35.9	0.093	0.330	3.55
Glenn	84	Male	20.4	0.123	0.305	2.48

SAR, specific absorption rate.

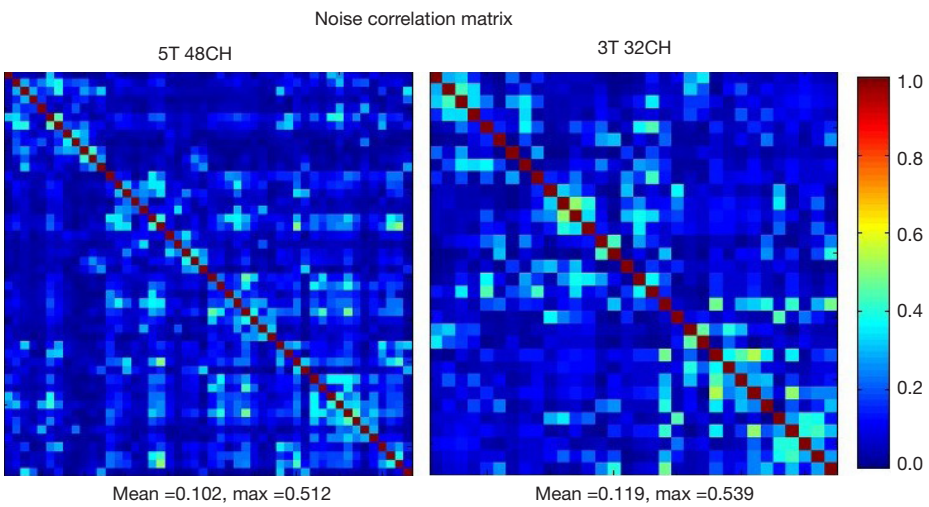

Figure 4 Noise correlation matrix of the 48-channel receiver coil at 5T and the 32-channel receiver coil at 3T in human studies. The maximum and mean value of the noise correlation matrix with exception for the diagonal elements are shown below the maps.

43 and 44) had an average value of –17 dB at 210.8 MHz, of which the worst-case situation was –14 dB. The isolation between the tuned and detuned states of the active detuning was nearly 40 dB. These results indicated that the tuning, matching, decoupling and detuning were satisfactory for the imaging requirements.

Figure 4 depicts the noise correlation matrix of the 48-channel receiver coil at 5T and the 32-channel receiver coil at 3T. For the 48-channel head coil at 5T, the mean and maximum value of the noise correlation with exception for the diagonal elements were 10.2% and 51.2%, respectively. They were 11.9% and 53.9% for the 32-channel head coil at 3T, respectively. These results demonstrated that the 48-channel receiver coil at 5T had sufficient channel decoupling.

After correction for flip angle differences, the SNR maps of the human brain (*Figure 5*) and a human head phantom (Figure S1) in the transversal, sagittal and coronal planes

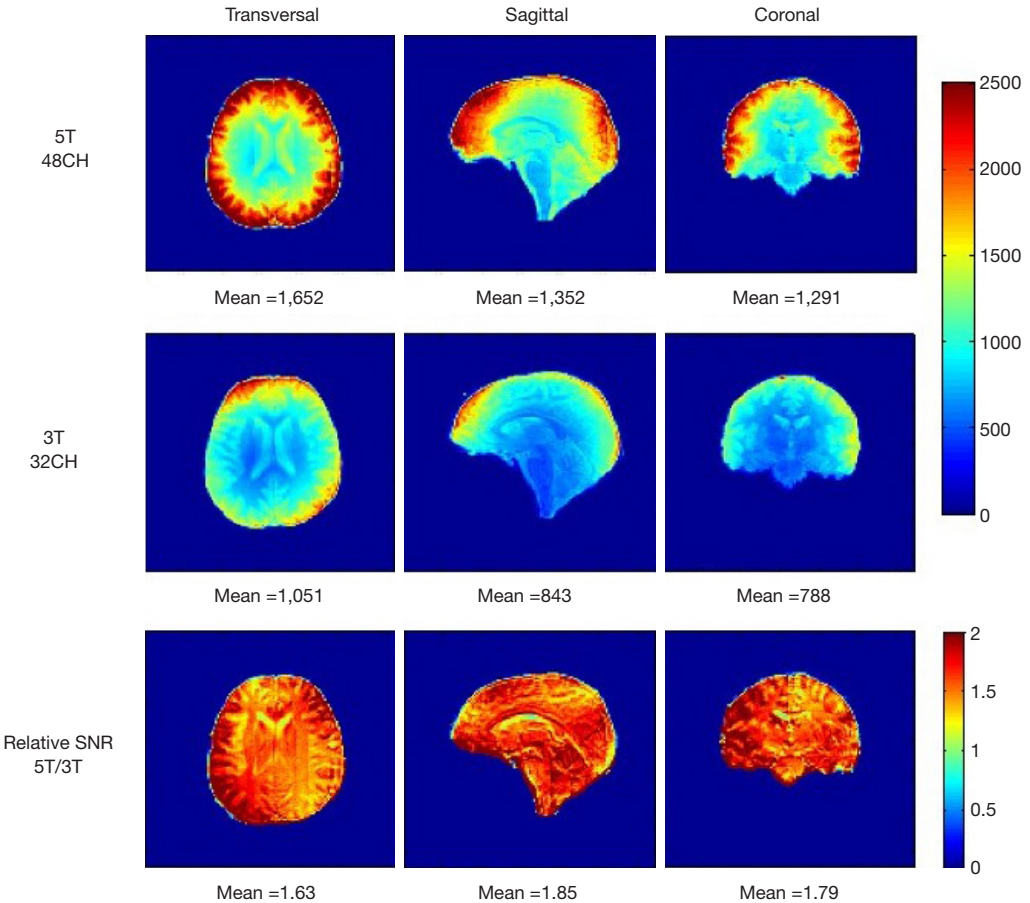

Figure 5 Signal-to-noise ratio (SNR) maps after correction for flip angle differences from a healthy volunteer (39 years old; male; 160 cm; 65 kg) at 5T and 3T. Mean values for SNR in the brain regions are displayed below each image. Relative SNR differences (5T/3T) between the SNR maps are shown at the bottom.

acquired at the 5T and 3T MRI scanners are shown. The mean SNR values in the brain regions were calculated and shown below the corresponding maps. As indicated by the mean values in *Figure 5*, the average SNR values in the transversal, sagittal, and coronal planes at 5T are 1.63 times, 1.85 times, and 1.79 times of those at 3T, respectively. These values corresponded with those of the phantom (1.90 times, 1.83 times, and 1.79 times, respectively, as shown in Figure S1 and Appendix 1). In the T2* measurements, the T2* values of the white and gray matter at 5T were 29.3 and 40.3 ms, while the corresponding values at 3T were 43.5 and 62.0 ms. In the T1 measurements, the T1 values of the white and gray matter at 5T were 1218 ms and 1883 ms, while the corresponding values at 3T were 955 ms and 1571 ms. These results are consistent with those found by Pohmann (9). After correction for T1, T2* (using the values of the white matter) and flip angle differences, the average SNR values in the transversal, sagittal, and coronal planes of the brain at 5T were 1.76 times, 2 times and 1.93 times of those at 3T, respectively.

The inverse g-factor maps with various SENSE acceleration factors in the transverse plane are shown in *Figure 6*. The mean and maximum 1/g-factor values in the indicated ROI were displayed below the corresponding maps. The 48-channel head coil at 5T demonstrated lower g-factors than the 32-channel head coil at 3T, particularly at a high acceleration factor, achieving a better performance in the imaging acceleration capacity.

Figure 7 depicts the T2-weighted FSE images of a healthy volunteer at 5T and 3T. The 300 μm in-plane resolution image from the 5T MRI scan shows the hippocampus in fine detail. The hippocampus is related to amnesia and dementia. The increased magnification of an area within the images better illustrates the higher quality

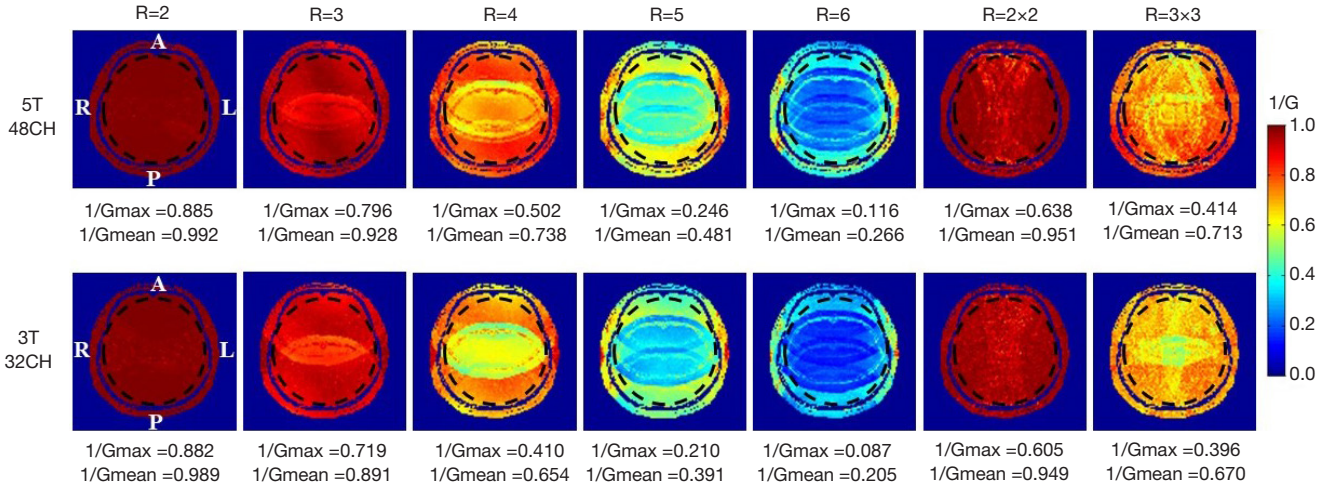

Figure 6 The inverse g-factor maps in the transversal plane of the human brain obtained by a two-dimensional density-weighted gradient echo (GRE) sequence from a healthy volunteer (39 years old; male; 160 cm; 65 kg) at 5T and 3T. Maximum and mean values in the regions of interest identified with the dashed ellipses are displayed below each image.

of the hippocampal head, hippocampal body, hippocampal tail, and mesencephalon at 5T compared to 3T.

MRA images demonstrated that the 5T MRI scanner provided better image quality than that of the 3 T MRI scanner (*Figure 8*). An increased number of vessels was observed at 5T compared to 3T because of the higher SNR. Improved delineation of LSAs was observed at 5T compared to 3T, especially in the more distal vessels (*Figure 8C*).

Figure 9 and *Figure 10* show the vascular wall images of LSAs and basilar arteries, respectively. More distal vessels of LSAs were observed at 5T compared to 3T (*Figure 9*). The delineation of these LSAs allows for visualizing normal vessels and detecting possible pathologies such as arterial dissection and small LSA aneurysms. Basilar arteries with improved delineation and reduced blurring can be appreciated at 5T compared to 3T (*Figure 10*).

SWI revealed the difference in veins of deep brain regions between 5T and 3T scans (*Figure 11*). More details of veins were observed at 5T compared to 3T with the same acquired resolution of 0.5×0.5×1.0 mm^3. At 5T, SWI images with a higher resolution of 0.3×0.3×1.2 mm^3 were also obtained, which showed more vessels and details than the SWI images with an acquired resolution of 0.5×0.5 ×1.0 mm^3.

Discussion

In the simulations study, the 5T MRI showed more homogeneous B_1^+ field distributions than those shown by the 7 T MRI, as observed in *Figure 2*. In the human head model (Gustav), the B_1^+ field homogeneity at 5T could be improved by more than 26%. Compared to the 3T MRI using the 32-channel head coil, the 5T MRI using the 48-channel head coil demonstrated higher SNR and a better parallel imaging performance. These findings demonstrate that 5T MRI can provide significant signal-to-noise ratio improvement compared to that of 3T MRI with less RF inhomogeneity than that of 7T MRI.

Pohmann's study (9) assumed a relationship of $SNR \sim B_0^{1.65}$, which was calculated for the cerebrum by fitting three points. But it may deviate in the whole brain evaluation. For example, the increase of SNR at 7T compared to that of 3T is 4.00 based on this relationship. However, the SNR increase from 3T to 7T is with 2.96±0.22, 3.36±0.24, and 3.78±0.37 in the outer brain region, in the inner brain and the cerebellum, respectively. These values are also lower than those calculated by the theoretical estimation. The increase of SNR at 5T (210.8 MHz) compared with that at 3T (128.2 MHz) is 2.27 based on this relationship. The measured increase in the average values in the transversal, sagittal, and coronal planes of the human brain at 5T are 1.76, 2 and 1.93, which could be within the margin of error.

Our findings showed that the 5T MRI can provide high-resolution anatomic images, angiography images, vessel wall images, and SWI. The images were compared with those acquired on a commercial 3T MRI scanner, which showed

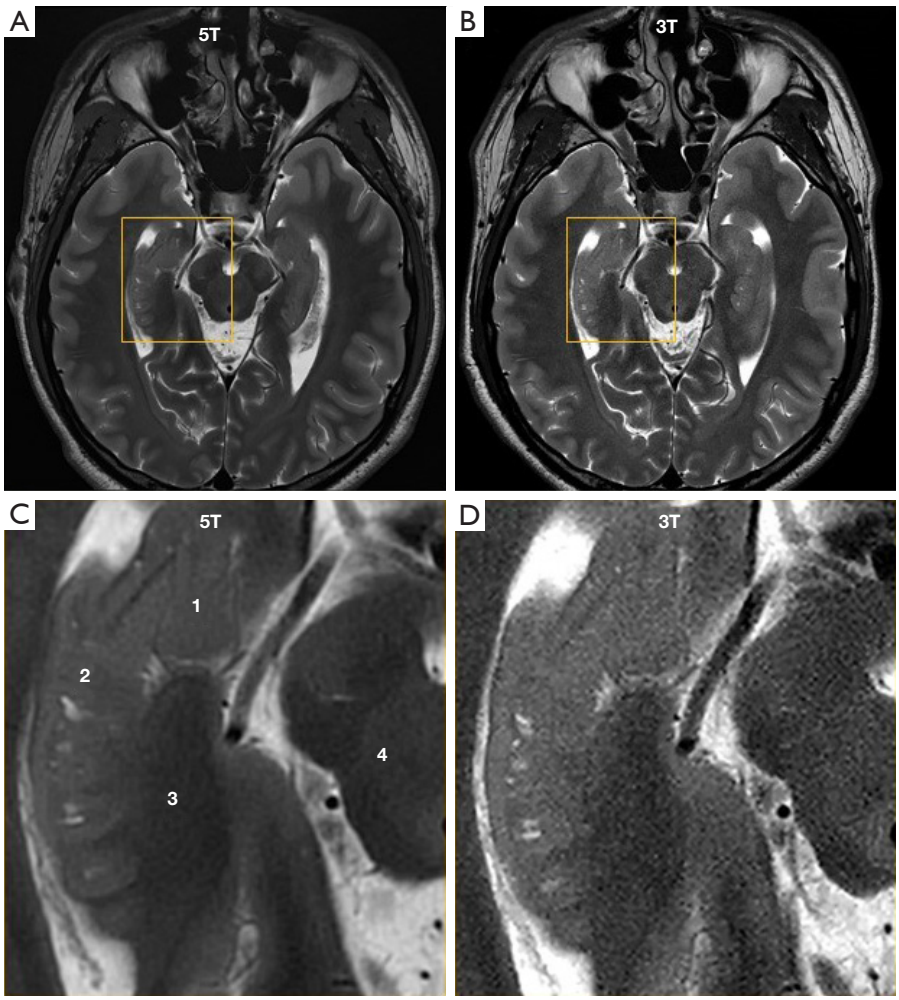

Figure 7 T2-weighted fast spin echo brain images of a healthy volunteer (37 years old; male; 170 cm; 70 kg). The images were acquired with an acquired resolution of 0.3 mm × 0.3 mm × 2.5 mm at 5T (A) and 3T (B). Magnification of the hippocampal area (yellow rectangles) from the 5T image (C) and the 3T image (D). 1: hippocampal head; 2: hippocampal body; 3: hippocampal tail; 4: mesencephalon.

that the image quality using 5T was better compared to that obtained using 3T MRI. Particularly, the hippocampus could be better illustrated at 5T MRI compared to 3T MRI. Improved delineation of lenticulostriate arteries and basilar arteries associated with ischemic stroke was observed at 5T MRI compared to 3T MRI. SWI images with a higher acquired resolution of 0.3×0.3×1.2 mm^3 could be obtained using the 5T MRI scanner, which showed more small blood vessels compared to those using the 3 T MRI scanner. This improved imaging can assist in assessing cerebral veins, stroke, multiple sclerosis, tumors and hemorrhagic lesions.

The 5T MRI shows a more homogenous B_1^+ field and has fewer safety issues related to SAR problems compared to the 7T MRI. Therefore, using the quadrature birdcage coil can achieve good performance at 5T. Undeniably, using parallel transmit techniques could potentially improve the B_1^+ field homogeneity and reduce RF energy deposition. So far, for the human brain imaging at 7 T, only the quadrature birdcage transmit coil integrated with a 32-channel receiver head coil has been approved by FDA (52). Currently, the parallel transmit coils are only permitted for use in the nondiagnostic research mode and are not cleared for the CE-labeled clinical mode at the latest generation 7T systems (53). Some studies show that radiative antenna arrays may have advantages over more conventional coil array elements when imaging deeply located body targets at ultrahigh field MRI (54-56), such as monopole antenna (54), dipole antenna (55) and J-shape antenna (56). Further work

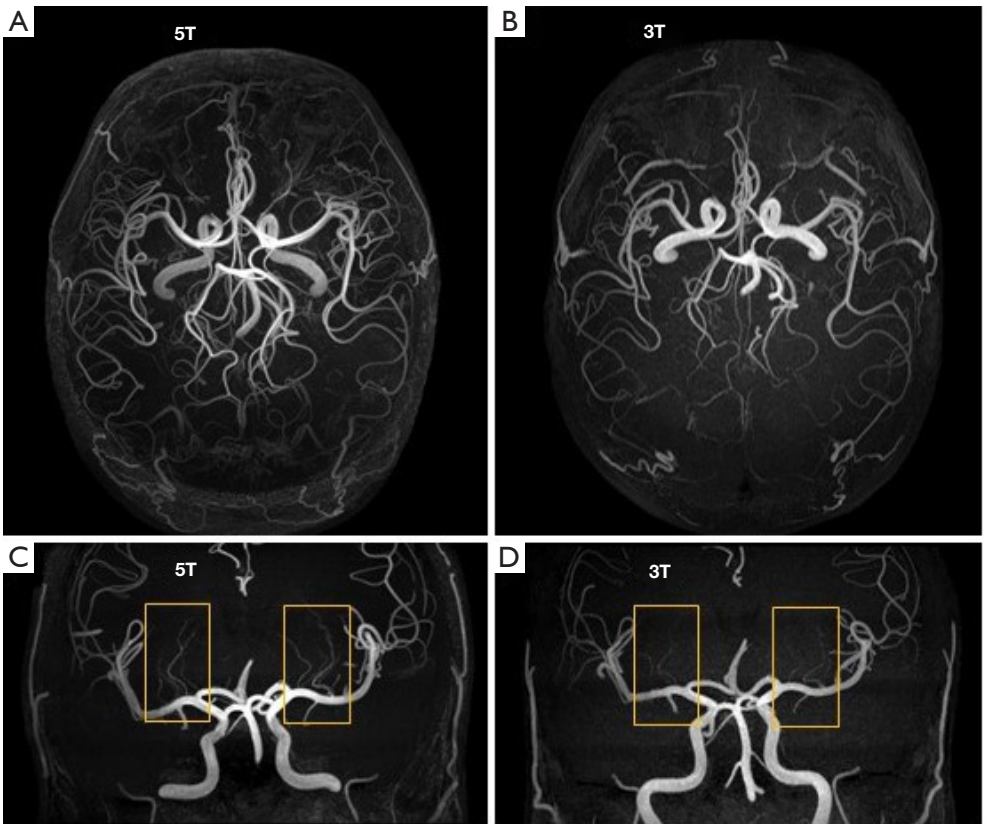

Figure 8 Magnetic resonance angiography images obtained by a time of flight sequence of a healthy volunteer (28 years old; male; 170 cm; 52 kg). Vessels in the brain were imaged with a 0.5 mm × 0.5 mm × 0.5 mm acquired resolution at 5T (A) and 3T (B). Lenticulostriate arteries (yellow rectangles) were observed at 5T (C) and 3T (D).

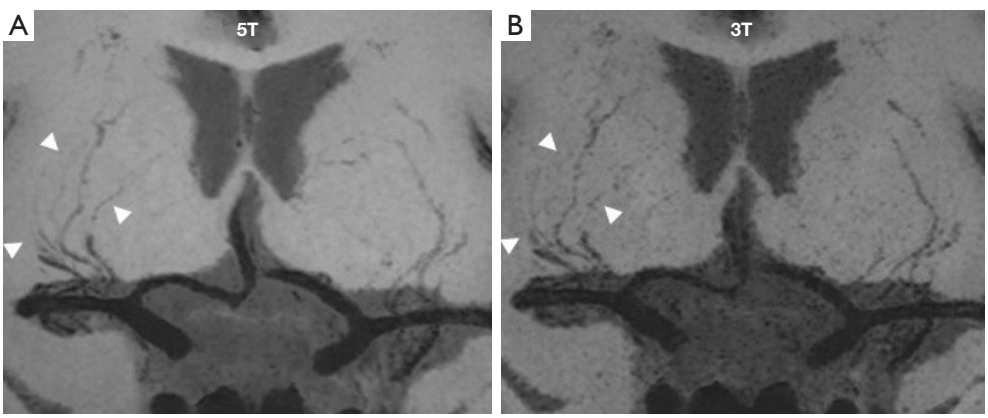

Figure 9 Vascular wall images of Lenticulostriate arteries (LSAs) from obtained by a T1-weighted three-dimensional MATRIX sequence a healthy volunteer (39 years old; male; 170 cm; 80 kg). Thin minimum intensity projection across 10 mm slices for the visualization of LSAs at 5T (A) and 3T (B). Distal vessels were better observed at 5T than at 3T, as shown by the white arrow heads. LSAs, lenticulostriate arteries; MATRIX, Modulated flip Angle Technique in Refocused Imaging with eXtended echo train.

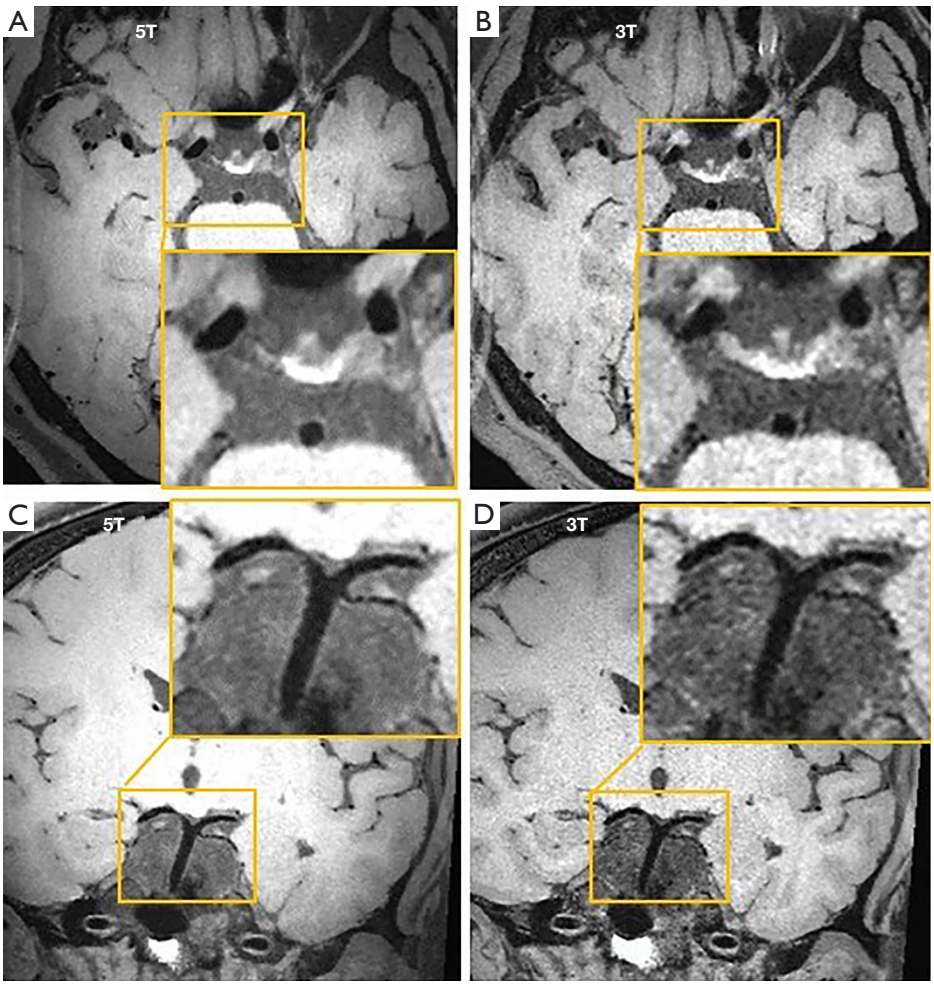

Figure 10 Vascular wall images of basilar arteries obtained by a T1-weighted three-dimensional MATRIX sequence from a healthy volunteer (39 years old; male; 170 cm; 80 kg). The images were obtained with a 0.5 mm × 0.5 mm × 0.5 mm reconstructed resolution for 5T (A,C) and 3T (B,D). Magnification of areas in the brain (yellow rectangles) at 5T and 3T are also displayed. MATRIX, Modulated flip Angle Technique in Refocused Imaging with eXtended echo train.

is needed on the parallel transmit techniques and radiative antenna arrays at 5T MRI.

To improve the transmit efficient, the local transmit birdcage coils for human brain imaging are usually shielded, which lead to the coils hindering access to the imaging participants. This structure reduces the participant's comfort and makes the MRI examination stressful, especially for claustrophobic patients. A large window in front of the participant's face would help during cognitive functional MRI experiments (57). To provide a large opening in front of the participant's face, various open transmit coils are available, such as half-birdcage coils (58), U-shaped birdcage coils (59), quadrature half-volume transverse electromagnetic coils (60) and open birdcage coil (61). Further work is needed on open transmit coils at 5T MRI to achieve this outcome.

The 5T MRI scanner has a lighter weight during operation than the 7T MRI. The 5T MRI scanner weighs 17 tons in operation with a 60 cm diameter bore size and a 206 cm magnet length, while the commercial 7T MRI scanner (MAGNETOM Terra, Siemens) weighs less than 25 tons in operation with a 60 cm diameter bore size and a 270 cm magnet length. The 5 Gauss line for the 5T MRI scanner is 4.10 m × 3.60 m, a reduction of 37% compared to the 5 Gauss lines of the 7T MRI scanner, which is 8.00 m × 5.00 m. However, the distance of the 5 Gauss line depends

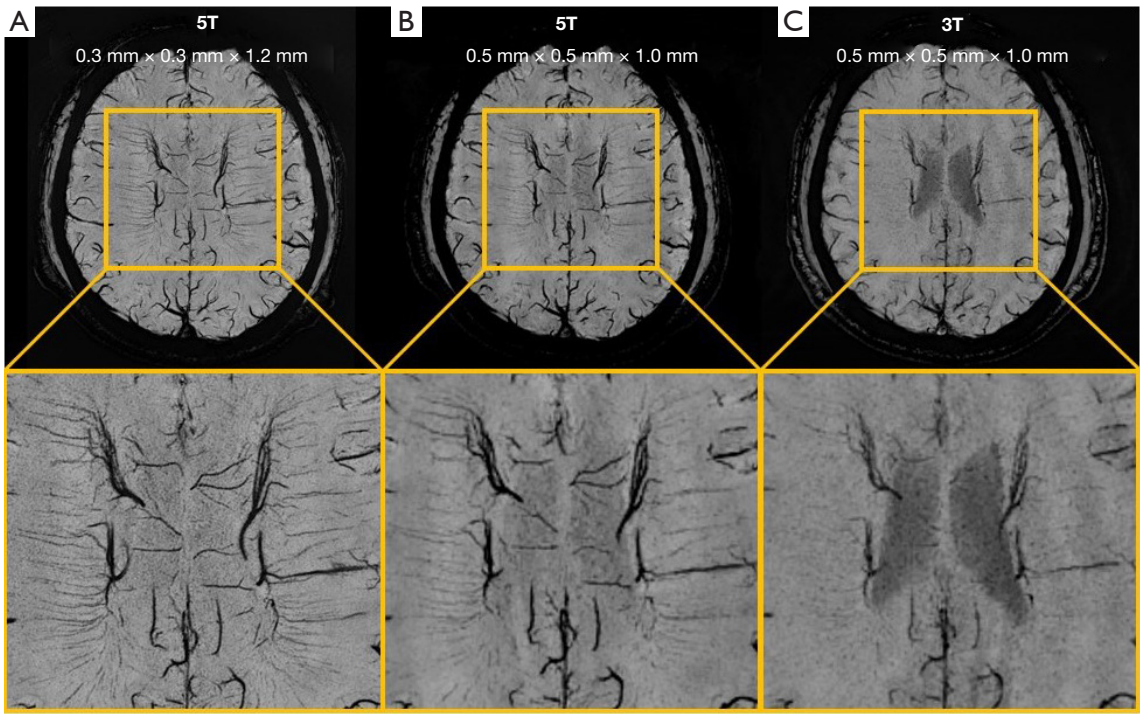

Figure 11 The minimum intensity projection of susceptibility weighted images from a healthy volunteer (39 years old; male; 170 cm; 80 kg). The images were obtained with a 0.3 mm × 0.3 mm × 1.2 mm acquired resolution for 5T (A), and a 0.5 mm × 0.5 × 1.0 mm acquired resolution for 5T (B) and 3T (C) scans. Magnification of areas in the brain (yellow rectangles) at 5T and 3T is also displayed.

on the magnet technology and active shielding.

Whole-body imaging at 4T has been investigated since the late 1980s (62,63). Using a transmit/receive four-port drive birdcage RF coil, the images acquired at 4 T were not optimal. In 2001, body imaging results acquired with birdcage transmit coils and phased array receiver coils indicate that 3T whole-body systems have a clinical role (64), which greatly impacted 4T MRI. Since then, research has focused on 3T and 7T MRI studies. Additionally, some diffusion scans implemented with 40 mT/m, 80 mT/m and 120 mT/m gradient (Figure S2 and Appendix 1) at 5 T demonstrated that the stronger the gradient strength, the shorter the TE and the higher the SNR. Therefore, with the continued development of high-performance gradient systems, high-performance whole-body transmit coils, high-density receiver coils and fast imaging techniques, 5T MRI can potentially achieve better image quality than that of the earlier 4T MRI.

Conclusions

In conclusion, the quadrature birdcage transmit/48-channel receiver coil assembly at 5T obtained an improved SNR and higher quality human brain images compared to those of the 32-channel head coil at 3T. In particular, high-resolution SWI phase imaging at 5T had impressive anatomical contrast. The 5T MRI scanner using the quadrature birdcage transmit/48-channel receiver coil assembly has potential clinical and brain science applications. It may significantly impact the diagnoses, prognoses, and treatment of neurological diseases. Future work will include confirmation of our results and performance evaluations in SWI.

Acknowledgments

Funding: This work was supported by the National Key Research and Development Program of China (No. 2021YFE0204400 to Y Li and No. 2021YFC2400203 to Q Chen); the Strategic Priority Research Program of Chinese Academy of Sciences (No. XDB25000000 to H Zheng); National Natural Science Foundation of China (No. 62125111 to D Liang and No. 52293425 to H Zheng); Special Project on Global Common Challenges of Chinese

Academy of Sciences (No. 321GJHZ2022081GC to Y Li); Youth Innovation Promotion Association of CAS (No. Y2021098 to Y Li); Key Laboratory Project of Guangdong Province (No. 2020B1212060051 to X Liu); Shenzhen City Grant (No. RCYX20200714114735123 to Y Li).

Footnote

Conflicts of Interest: All authors have completed the ICMJE uniform disclosure form (available at https://qims.amegroups.com/article/view/10.21037/qims-22-945/coif). DL serves as an unpaid editorial board member of *Quantitative Imaging in Medicine and Surgery* and reports that his institution was funded by National Natural Science Foundation of China (No. 62125111). XZ serves as an unpaid Associate Editor of *Quantitative Imaging in Medicine and Surgery*. YL reports that his institution was funded by the National Key Research and Development Program of China (No. 2021YFE0204400); Special Project on Global Common Challenges of Chinese Academy of Sciences (No. 321GJHZ2022081GC); Youth Innovation Promotion Association of CAS (No. Y2021098); and Shenzhen City Grant (No. RCYX20200714114735123). QC reports that her institution was funded by the National Key Research and Development Program of China (No. 2021YFC2400203). HZ reports that his institution was funded by the Strategic Priority Research Program of Chinese Academy of Sciences (No. XDB25000000) and National Natural Science Foundation of China (No. 52293425). XL reports that his institution was funded by Key Laboratory Project of Guangdong Province (No. 2020B1212060051). ZW received financial support from Shanghai United Imaging Healthcare Co., Ltd. Shihong Han, Shuheng Zhang, Haining Wang, Qiang He are employees of Shanghai United Imaging Healthcare Co., Ltd. The other authors have no conflicts of interest to declare.

Ethical Statement: The authors are accountable for all aspects of the work by ensuring that questions related to the accuracy or integrity of any part of the work are appropriately investigated and resolved. This study conformed to the provisions of the Declaration of Helsinki (as revised in 2013). The study was approved by the institutional review board of Shenzhen Institutes of Advanced Technology, Chinese Academy of Sciences. Before the human studies were initiated, informed consent was obtained from all of the volunteers.

References

1. Global, regional, and national burden of neurological disorders, 1990-2016: a systematic analysis for the Global Burden of Disease Study 2016. Lancet Neurol 2019;18:459-80.
2. Harisinghani MG, O'Shea A, Weissleder R. Advances in clinical MRI technology. Sci Transl Med 2019;11:eaba2591.
3. De Feyter HM, Behar KL, Corbin ZA, Fulbright RK, Brown PB, McIntyre S, Nixon TW, Rothman DL, de Graaf RA. Deuterium metabolic imaging (DMI) for MRI-based 3D mapping of metabolism in vivo. Sci Adv 2018;4:eaat7314.
4. Rich LJ, Bagga P, Wilson NE, Schnall MD, Detre JA, Haris M, Reddy R. (1)H magnetic resonance spectroscopy of (2)H-to-(1)H exchange quantifies the dynamics of cellular metabolism in vivo. Nat Biomed Eng 2020;4:335-42.
5. He X, Ertürk MA, Grant A, Wu X, Lagore RL, DelaBarre L, Eryaman Y, Adriany G, Auerbach EJ, Van de Moortele PF, Uğurbil K, Metzger GJ. First in-vivo human imaging at 10.5T: Imaging the body at 447 MHz. Magn Reson Med 2020;84:289-303.
6. Platt T, Ladd ME, Paech D. 7 Tesla and Beyond: Advanced Methods and Clinical Applications in Magnetic Resonance Imaging. Invest Radiol 2021;56:705-25.
7. Bangerter NK, Taylor MD, Tarbox GJ, Palmer AJ, Park DJ. Quantitative techniques for musculoskeletal MRI at 7 Tesla. Quant Imaging Med Surg 2016;6:715-30.
8. Okada T, Fujimoto K, Fushimi Y, Akasaka T, Thuy DHD, Shima A, Sawamoto N, Oishi N, Zhang Z, Funaki T, Nakamoto Y, Murai T, Miyamoto S, Takahashi R, Isa T. Neuroimaging at 7 Tesla: a pictorial narrative review. Quant Imaging Med Surg 2022;12:3406-35.
9. Pohmann R, Speck O, Scheffler K. Signal-to-noise ratio and MR tissue parameters in human brain imaging at 3, 7, and 9.4 tesla using current receive coil arrays. Magn Reson

Med 2016;75:801-9.
10. Natsumeda M, Matsuzawa H, Watanabe M, Motohashi K, Gabdulkhaev R, Tsukamoto Y, Kanemaru Y, Watanabe J, Ogura R, Okada M, Kurabe S, Okamoto K, Kakita A, Igarashi H, Fujii Y. SWI by 7T MR Imaging for the Microscopic Imaging Diagnosis of Astrocytic and Oligodendroglial Tumors. AJNR Am J Neuroradiol 2022;43:1575-81.
11. Deistung A, Rauscher A, Sedlacik J, Stadler J, Witoszynskyj S, Reichenbach JR. Susceptibility weighted imaging at ultra high magnetic field strengths: theoretical considerations and experimental results. Magn Reson Med 2008;60:1155-68.
12. Seo JH, Chung JY. A Preliminary Study for Reference RF Coil at 11.7 T MRI: Based on Electromagnetic Field Simulation of Hybrid-BC RF Coil According to Diameter and Length at 3.0, 7.0 and 11.7 T. Sensors (Basel) 2022;22:1512.
13. Deelchand DK, Van de Moortele PF, Adriany G, Iltis I, Andersen P, Strupp JP, Vaughan JT, Uğurbil K, Henry PG. In vivo 1H NMR spectroscopy of the human brain at 9.4 T: initial results. J Magn Reson 2010;206:74-80.
14. Ertürk MA, Wu X, Eryaman Y, Van de Moortele PF, Auerbach EJ, Lagore RL, DelaBarre L, Vaughan JT, Uğurbil K, Adriany G, Metzger GJ. Toward imaging the body at 10.5 tesla. Magn Reson Med 2017;77:434-43.
15. Yang QX, Wang J, Zhang X, Collins CM, Smith MB, Liu H, Zhu XH, Vaughan JT, Ugurbil K, Chen W. Analysis of wave behavior in lossy dielectric samples at high field. Magn Reson Med 2002;47:982-9.
16. Van de Moortele PF, Akgun C, Adriany G, Moeller S, Ritter J, Collins CM, Smith MB, Vaughan JT, Uğurbil K. B(1) destructive interferences and spatial phase patterns at 7 T with a head transceiver array coil. Magn Reson Med 2005;54:1503-18.
17. Williams SN, McElhinney P, Gunamony S. Ultra-high field MRI: parallel-transmit arrays and RF pulse design. Phys Med Biol 2023.
18. Pang Y, Yu B, Vigneron DB, Zhang X. Quadrature transmit array design using single-feed circularly polarized patch antenna for parallel transmission in MR imaging. Quant Imaging Med Surg 2014;4:11-8.
19. Herrler J, Williams SN, Liebig P, Ding B, McElhinney P, Allwood-Spiers S, Meixner CR, Gunamony S, Maier A, Dörfler A, Gumbrecht R, Porter DA, Nagel AM. The effects of RF coils and SAR supervision strategies for clinically applicable nonselective parallel-transmit pulses at 7 T. Magn Reson Med 2023;89:1888-900.
20. Katscher U, Börnert P, Leussler C, van den Brink JS. Transmit SENSE. Magn Reson Med 2003;49:144-50.
21. Katscher U, Börnert P, van den Brink JS. Theoretical and numerical aspects of transmit SENSE. IEEE Trans Med Imaging 2004;23:520-5.
22. Grissom W, Yip CY, Zhang Z, Stenger VA, Fessler JA, Noll DC. Spatial domain method for the design of RF pulses in multicoil parallel excitation. Magn Reson Med 2006;56:620-9.
23. Zhang Z, Yip CY, Grissom W, Noll DC, Boada FE, Stenger VA. Reduction of transmitter B1 inhomogeneity with transmit SENSE slice-select pulses. Magn Reson Med 2007;57:842-7.
24. Zelinski AC, Wald LL, Setsompop K, Alagappan V, Gagoski BA, Goyal VK, Adalsteinsson E. Fast slice-selective radio-frequency excitation pulses for mitigating B+1 inhomogeneity in the human brain at 7 Tesla. Magn Reson Med 2008;59:1355-64.
25. Setsompop K, Alagappan V, Gagoski BA, Potthast A, Hebrank F, Fontius U, Schmitt F, Wald LL, Adalsteinsson E. Broadband slab selection with B1+ mitigation at 7T via parallel spectral-spatial excitation. Magn Reson Med 2009;61:493-500.
26. Wu X, Schmitter S, Auerbach EJ, Uğurbil K, Van de Moortele PF. Mitigating transmit B 1 inhomogeneity in the liver at 7T using multi-spoke parallel transmit RF pulse design. Quant Imaging Med Surg 2014;4:4-10.
27. Schmitter S, DelaBarre L, Wu X, Greiser A, Wang D, Auerbach EJ, Vaughan JT, Uğurbil K, Van de Moortele PF. Cardiac imaging at 7 Tesla: Single- and two-spoke radiofrequency pulse design with 16-channel parallel excitation. Magn Reson Med 2013;70:1210-9.
28. Cloos MA, Boulant N, Luong M, Ferrand G, Giacomini E, Le Bihan D, Amadon A. kT -points: short three-dimensional tailored RF pulses for flip-angle homogenization over an extended volume. Magn Reson Med 2012;67:72-80.
29. Moser E, Laistler E, Schmitt F, Kontaxis G. Ultra-high field NMR and MRI-the role of magnet technology to increase sensitivity and specificity. Front Phys 2017;5:33.
30. Vaughan JT, Garwood M, Collins CM, Liu W, DelaBarre L, Adriany G, Andersen P, Merkle H, Goebel R, Smith MB, Ugurbil K. 7T vs. 4T: RF power, homogeneity, and signal-to-noise comparison in head images. Magn Reson Med 2001;46:24-30.
31. Ibrahim TS, Hue YK, Tang L. Understanding and manipulating the RF fields at high field MRI. NMR Biomed 2009;22:927-36.

32. Chen H, Guo L, Li M, Destruel A, Liu C, Weber E, Liu F, Crozier S. Metamaterial-Inspired Radiofrequency (RF) Shield With Reduced Specific Absorption Rate (SAR) and Improved Transmit Efficiency for UHF MRI. IEEE Trans Biomed Eng 2021;68:1178-89.
33. Hoffmann J, Henning A, Giapitzakis IA, Scheffler K, Shajan G, Pohmann R, Avdievich NI. Safety testing and operational procedures for self-developed radiofrequency coils. NMR Biomed 2016;29:1131-44.
34. International Electrotechnical Commission (IEC). Particular requirements for the basic safety and essential performance of magnetic resonance equipment for medical diagnosis. Medical electrical equipment. London, England: IEC, 541 (2015).
35. Hennig J. Ultra high field MR: useful instruments or toys for the boys. MAGMA 2008;21:1-3.
36. De Vita E, Thomas DL, Roberts S, Parkes HG, Turner R, Kinchesh P, Shmueli K, Yousry TA, Ordidge RJ. High resolution MRI of the brain at 4.7 Tesla using fast spin echo imaging. Br J Radiol 2003;76:631-7.
37. Thomas DL, De Vita E, Roberts S, Turner R, Yousry TA, Ordidge RJ. High-resolution fast spin echo imaging of the human brain at 4.7 T: implementation and sequence characteristics. Magn Reson Med 2004;51:1254-64.
38. Keil B, Wald LL. Massively parallel MRI detector arrays. J Magn Reson 2013;229:75-89.
39. Ryu KH, Baek HJ, Moon JI, Choi BH, Park SE, Ha JY, Jeon KN, Bae K, Choi DS, Cho SB, Lee Y, Heo YJ. Initial clinical experience of synthetic MRI as a routine neuroimaging protocol in daily practice: A single-center study. J Neuroradiol 2020;47:151-60.
40. Zhu H, Yang X, Wyban M, Guan Y, Hamamura Y, Takano Y, Okamoto K. A 64-channel phased-array head neck coil for neurovascular/fMRI at 3T. Proc Intl Soc Mag Reson Med 2019;27:1525.
41. Lattanzi R, Wiggins GC, Zhang B, Duan Q, Brown R, Sodickson DK. Approaching ultimate intrinsic signal-to-noise ratio with loop and dipole antennas. Magn Reson Med 2018;79:1789-803.
42. Guérin B, Villena JF, Polimeridis AG, Adalsteinsson E, Daniel L, White JK, Wald LL. The ultimate signal-to-noise ratio in realistic body models. Magn Reson Med 2017;78:1969-80.
43. Vaidya MV, Sodickson DK, Lattanzi R. Approaching Ultimate Intrinsic SNR in a Uniform Spherical Sample with Finite Arrays of Loop Coils. Concepts Magn Reson Part B Magn Reson Eng 2014;44:53-65.
44. Ianniello C, de Zwart JA, Duan Q, Deniz CM, Alon L, Lee JS, Lattanzi R, Brown R. Synthesized tissue-equivalent dielectric phantoms using salt and polyvinylpyrrolidone solutions. Magn Reson Med 2018;80:413-9.
45. Li Y, Chen Q, Wei Z, Zhang L, Tie C, Zhu Y, Jia S, Xia J, Liang D, He Q, Zhang X, Liu X, Zhang B, Zheng H. One-Stop MR Neurovascular Vessel Wall Imaging With a 48-Channel Coil System at 3 T. IEEE Trans Biomed Eng 2020;67:2317-27.
46. Gabriel S, Lau RW, Gabriel C. The dielectric properties of biological tissues: III. Parametric models for the dielectric spectrum of tissues. Phys Med Biol 1996;41:2271-93.
47. Giovannetti G, Hartwig V, Positano V, Vanello N. Radiofrequency coils for magnetic resonance applications: theory, design, and evaluation. Crit Rev Biomed Eng 2014;42:109-35.
48. Roemer PB, Edelstein WA, Hayes CE, Souza SP, Mueller OM. The NMR phased array. Magn Reson Med 1990;16:192-225.
49. Pruessmann KP, Weiger M, Scheidegger MB, Boesiger P. SENSE: sensitivity encoding for fast MRI. Magn Reson Med 1999;42:952-62.
50. Fewel ME, Thompson BG Jr, Hoff JT. Spontaneous intracerebral hemorrhage: a review. Neurosurg Focus 2003;15:E1.
51. International Electrotechnical Commission (IEC). Particular requirements for the safety of magnetic resonance equipment for medical diagnosis. International Standard IEC 60601-2-33. Geneva, Switzerland: IEC; 2010.
52. U.S. Food and Drug Administration. FDA Clears First 7T Magnetic Resonance Imaging Device (FDA Web site). October 12, 2017. Available online: https://www.fda.gov/NewsEvents/Newsroom/PressAnnouncements/ucm58015htm.
53. Kraff O, Quick HH. Radiofrequency Coils for 7 Tesla MRI. Top Magn Reson Imaging 2019;28:145-58.
54. Hong SM, Park JH, Woo MK, Kim YB, Cho ZH. New design concept of monopole antenna array for UHF 7T MRI. Magn Reson Med 2014;71:1944-52.
55. Raaijmakers AJ, Italiaander M, Voogt IJ, Luijten PR, Hoogduin JM, Klomp DW, van den Berg CA. The fractionated dipole antenna: A new antenna for body imaging at 7 Tesla. Magn Reson Med 2016;75:1366-74.
56. Choi CH, Hong SM, Felder J, Tellmann L, Scheins J, Kops ER, Lerche C, Shah NJ. A Novel J-Shape Antenna Array for Simultaneous MR-PET or MR-SPECT Imaging. IEEE Trans Med Imaging 2022;41:1104-13.
57. Huang RS, Sereno MI. Visual stimulus presentation using

fiber optics in the MRI scanner. J Neurosci Methods 2008;169:76-83.
58. Ballon D, Graham MC, Miodownik S, Koutcher JA. A 64 MHz half-birdcage resonator for clinical imaging. J Magn Reson (1969) 1990;90:131-40.
59. Hudson AM, Köckenberger W, Bowtell RW. Open access birdcage coils for microscopic imaging of plants at 11.7 T. MAGMA 2000;10:69-74.
60. Peshkovsky AS, Kennan RP, Fabry ME, Avdievich NI. Open half-volume quadrature transverse electromagnetic coil for high-field magnetic resonance imaging. Magn Reson Med 2005;53:937-43.
61. Nikulin AV, Vignaud A, Avdievich NI, Berrahou D, de Rosny J, Ourir A. Open birdcage coil for head imaging at 7T. Magn Reson Med 2021;86:2290-300.
62. Barfuss H, Fischer H, Hentschel D, Ladebeck R, Vetter J. Whole-body MR imaging and spectroscopy with a 4-T system. Radiology 1988;169:811-6.
63. Bomsdorf H, Helzel T, Kunz D, Röschmann P, Tschendel O, Wieland J. Spectroscopy and imaging with a 4 tesla whole-body MR system. NMR Biomed 1988;1:151-8.
64. Watkins RD, Rohling KW, Piel J, Rosenfeld D, Kelley D, Lenkinski R, Kressel H, Montag A. Whole body RF coil for 3 Tesla MRI system. Proc Intl Soc Mag Reson Med 2001;9:1123.

Cite this article as: Wei Z, Chen Q, Han S, Zhang S, Zhang N, Zhang L, Wang H, He Q, Cao P, Zhang X, Liang D, Liu X, Li Y, Zheng H. 5T magnetic resonance imaging: radio frequency hardware and initial brain imaging. Quant Imaging Med Surg 2023;13(5):3222-3240. doi: 10.21037/qims-22-945

Appendix 1

Some signal-to-noise ratio (SNR) measurements were carried out on a human head phantom, which is filled with 1.24 g/L $NiSO_4 \cdot 6H_2O$ and 2.62 g/L NaCl. The signal images were acquired using a two-dimensional gradient echo (GRE) sequence (time of relaxation (TR) =3,000 ms; time of echo (TE) =6.5 ms; flip angle =30°; field of view (FOV) =250 mm × 250 mm; slice thickness =5 mm; matrix size =128×128; bandwidth =590 Hz/pixel). The noise images in each channel were obtained by setting the flip angle to zero. SNR was obtained using the following equation.

$$SNR^{\text{cov}-rSoS} = \sqrt{S^H \Psi^{-1} S} \quad [1]$$

where S is the signal image, H indicates transposed complex conjugate, and Ψ denotes the noise matrix.

The B_1^+ maps in the phantom were also evaluated using a dual refocusing echo acquisition mode (DREAM) sequence with the following parameters: TR =3,000 ms, TE =1.49 ms, flip angle =54.7°, slice thickness =10 mm, FOV= 250×250 mm^2, and matrix size =80×80.

The normalized SNR was calculated by using the formula: SNR/ sin (B_1^+), as shown in Figure S1. As shown by the mean values in the regions of interest, the average SNR values in the transversal, sagittal, and coronal planes at 5T were 1.90 times, 1.83 times, and 1.79 times of those at 3T, respectively. The average SNR values in the transversal, sagittal, and coronal planes of the human brain at 5T were 1.63 times, 1.85 times, and 1.79 times of those at 3T, respectively. These values corresponded with those of the phantom. The difference in the SNR results in the transversal plane might be caused by different slice positions. Nevertheless, the SNR results of the human brain corresponded with those of the phantom.

A diffusion scan was implemented with following parameters: TR =3,000 ms; TE =57.1 ms; flip angle =90°; slice thickness =5 mm; FOV = 220×230 mm^2; and matrix size =153×160; echo train length =51; bandwidth =1,750 Hz; b values: 0 sec/mm^2 and 3,000 sec/mm^2. In the diffusion scan, the shorter the TE, the stronger the gradient strength. We set the TE to the shortest value, corresponding to a 120 mT/m gradient. Additionally, we implemented two other diffusion scans with TE =61.9 ms and TE =79.9 ms, corresponding to a 40 mT/m and 80 mT/m gradient, respectively. The diffusion images and ADC images are shown in Figure S2. By dividing the signal by the quadrangle noise, the SNR in a region of interest of the diffusion image (b=3000) was obtained, as shown in Figure S2B. Compared to the SNR of the diffusion image (b=3000) using 40 mT/m, the SNR of the diffusion image (b=3000) using 120 mT/m increased by 42%. Compared to the SNR of the diffusion image (b=3000) using 80 mT/m, the SNR of the diffusion image (b=3000) using 120 mT/m increased by 10%. These results demonstrate that the stronger the gradient strength, the shorter the TE and the higher the SNR.

https://dx.doi.org/10.21037/qims-22-945

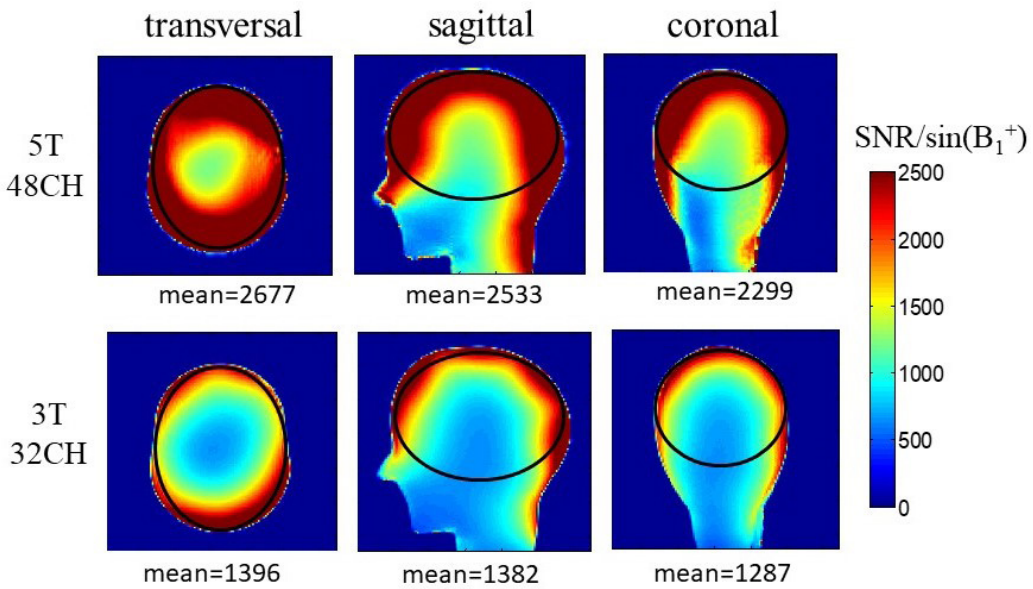

Figure S1 The normalized SNR maps of the phantom in the transversal, sagittal, and coronal planes at 5T and 3T.

https://dx.doi.org/10.21037/qims-22-945

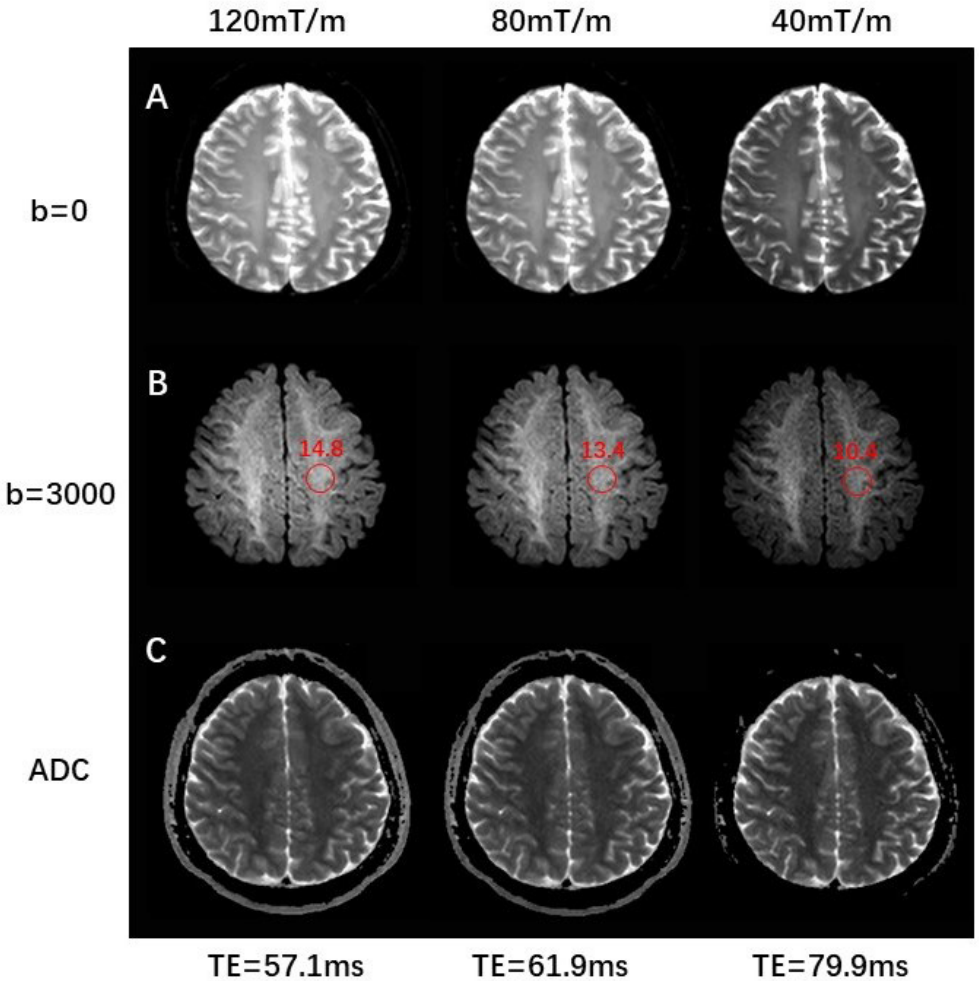

Figure S2 The diffusion images and apparent diffusion coefficient (ADC) images using different gradient strength at 5T MRI. The b3000 images are shown with an appropriate window level, while the other images are displayed with the same window levels.

https://dx.doi.org/10.21037/qims-22-945